ORIGINAL ARTICLE

Analysis of a two-layer cloud system with RAMS model and comparison to airborne observations

**Elias Mavromatidis · Theodoros I. Lekas ·
George Kallos**

Abstract A three-dimensional numerical model (Regional Atmospheric Modeling System—-RAMS) was used to study the formation and evolution of water forms in a two-layer cloud structure observed during a field campaign over Brest (France). The model performance in regular operations, using conventional meteorological data as initial and lateral boundary conditions, was also examined. Remote sensing observations of the cloud system and in-situ aircraft data, selected during the campaign, were used to validate the model outputs. The model simulations showed that the lower cloud formation was characterized by high number concentration of pristine ice and snow, while the concentration of aggregates, graupel and hail were considerably lower. Hydrometeors in liquid phase appeared demonstrating high number concentration and water content on the top of this layer. The upper cloud layer consisted only of frozen water substances in lower amounts. The qualitative and quantitative comparison of the model-calculated meteorological and microphysical fields to the available observational data revealed that the model reflected fairly well the cloud structure (e.g., the spatio-temporal variability of the cloud parameters, the geometry of the cloud system). However, there were deviations as far as the model underestimating the ice water content (IWC) and number concentration (N_t) fields is concerned, especially at the atmospheric layer between 2.5 and 4 km of altitude. These deviations of the model simulated quantities from the measured ones may be attributed either to the performance of the model's microphysics scheme, to instrument inaccuracies and to the local disturbance caused by the aircraft.

E. Mavromatidis · G. Kallos (✉)
School of Physics, Division of Applied Physics, National and Kapodistrian University of Athens,
University Campus, Bldg PHYS-5, 15784 Athens, Attika, Greece
e-mail: kallos@mg.uoa.gr

E. Mavromatidis
e-mail: imavr@mg.uoa.gr

Th. I. Lekas
Department of Aerodynamics and Flight Mechanics, Hellenic Air Force Academy, Dekelia Air Force
Base, TGA 1010 Dekelia, Attika, Greece
e-mail: lekas@mg.uoa.gr

1 Introduction

Clouds are an integral component of the earth's climate system. At any time clouds cover between 60 and 70% of the globe. They have a strong impact on solar and terrestrial radiation as well as on the formation of precipitation. In turn, the radiation and moisture fluxes in the atmosphere affect the formation and dissipation of clouds. During the recent years, it became possible to include more sophisticated cloud parameterizations into global, limited area and cloud models, mainly due to the rapidly increasing computer power. These schemes generally allow more realistic simulations of cloud processes at a variety of scales, as well as provide additional information about icing intensity and other weather phenomena, such as freezing rain/drizzle, mixed precipitation or blowing snow (Kain and Fritch [1], Tremback [2], Pielke et al. [3], Wang and Chang [4], Heckman and Cotton [5], Chen [6], Stevens et al. [7], Bernardet and Cotton [8], Harrington et al. [9], Wu et al. [10] and Jiang et al. [11,12] among others). For example, Stevens et al. [7] using the Regional Atmospheric Modeling System (RAMS) examined the influence of drizzle formation on the structure and dynamics of marine stratocumulus clouds. In another study, Bernardet and Cotton [8] simulated the evolution of an afternoon squall line into a derecho-producing nocturnal mesoscale convective system (MCS), while Wu et al. [10] examined the importance of radiative heating and cooling to the dynamics and microphysics of the 26 November 1991 FIRE II cirrus case described by Mace et al. [13].

A fundamental aspect concerning the development and improvement of forecasting systems and algorithms is their comparative verification through comparisons to in situ (often airborne) measurements (Brown et al. [14]). Since the influence of clouds on the earth's climate is quite complex, many studies have also been undertaken both with observations and with atmospheric models to get a better understanding of the formation of clouds and their interactions with the dynamics and radiation balance of the atmosphere. For instance, Guan et al. [15] projected model data on research aircraft trajectories to directly compare the model results with in situ aircraft measurements. In another work, aircraft measurements, collected through three research projects, were used to compare the forecasts from three explicit cloud schemes (Guan et al. [16]), whereas Nasiri et al. [17] examined the use of in-situ cirrus data to develop more complex midlatitude cirrus microphysical models. Furthermore, Lekas et al. [18] provided a theoretical calibration of optical array probes (OAP) mounted on a given aircraft combining an atmospheric modeling approach with a modeling approach through aircraft aerodynamics.

Some other studies evaluated the RAMS model at high resolutions. For example, Snook et al [19] and Powell and Rinard [20] discussed the local configuration and pointed error statistics for RAMS forecasts over the southeastern USA in support of weather forecasts for the 1996 Olympic Games, McQueen et al. [21] evaluated RAMS forecasts over the Chesapeake Bay against buoy observations, while Case et al. [22] presented an objective and a subjective verification of high-resolution RAMS forecasts over East-Central Florida during 1999 and 2002 summer months.

Many studies have been focused on the analysis of multilayered, overlapping cloud systems. Such cloud formations occur in more than half of cloud observations, as shown in the synoptic cloud observation studies by Warren et al. [23]. This type of clouds occurs commonly in the vicinity of fronts and also in the vicinity of deep tropical convection. In another study, performed over the North Atlantic Ocean, Tian and Curry [24] showed that the majority

of the multilayered cloud cases consisted of two-layer cloud systems at a spatial scale of approximately 45 km.

The current study analyzes a two-layer mixed-phase cloud structure through high resolution RAMS model simulations. The cloud studied was observed at 10 November 2000 during the second CARL field campaign and was chosen as the case study for model validation. The main objectives of the cloud analysis with the aid of the numerical atmospheric model were mainly to broaden our understanding of the microphysical and dynamical mechanisms which drives this type of cloud system and to provide insights about the strengths and weaknesses of the model microphysics scheme. The setting for the model simulation was over the Atlantic coastal region of Western France in the vicinity of Brest airport. Ground–based observations and in-situ aircraft data, which were obtained during the field campaign, have been used to validate the RAMS outputs, as well as to examine the spatiotemporal information that could be retrieved from the model simulations, especially concerning the water content (ice/IWC or liquid/LWC).

The remaining portion of the paper is organized as follows: Information concerning the observational data and an overview of the large-scale weather conditions, occurred during the experiment, are described in Sect. 2. A general description of the RAMS model is given in Sect. 3. Section 3 also includes the model configuration. The results of the model simulation are presented and compared to the observations in Sect. 4, together with an explanation proposed for the deviations. A summary and discussion are provided in Sect. 5.

2 Observations and large-scale weather condition

2.1 Observations

The second experimental campaign of the CARL project was set up for the time period between 6 and 24 November 2000 aiming to investigate mixed phase clouds alone and in multi-layered cloud systems. The experiment was performed at Brest airport, France, involving ground-based radar system, as well as in situ validation measurements collected by the Meteo-France 'Merlin IV' research aircraft. The aircraft was carrying the GKSS cloud particle measuring system (see Table 1). The data collected during the campaign was a joint effort of the other partners involved in this project (IPSL, GKSS, KNMI). The researchers of these groups are acknowledged for this work and for their courtesy to allow us the use of these data. The instrumentation and the methods used to retrieve the cloud properties, as well as more information about the experimental campaign are described in detail in Pelon et al. [25].

The experiment was accompanied by atmospheric model simulations on 10 November 2000. That day was characterized by low (stratocumulus) and middle-height clouds over the entire region of the western coast of France. The cloud structure captured by the radar showed that there were two main cloud layers. The upper cloud layer extended between 3 and 8 km and the lower one below 2 km, as it is illustrated in Fig. 1. In the lower cloud formation precipitation was found to occur in the vicinity of 0°C (at about an altitude of 1.2 km within the cloud), which designated the melting layer. A sudden increase in the particle falling velocities below this height, which is shown in radar data (Fig. 1c, d), indicates the transition from mixed phase water substances (ice/liquid water) into rain drops, which obtain much higher falling speeds.

Table 1 The characteristics of the cloud radar and the ranges of particle sizes of the GKSS probes

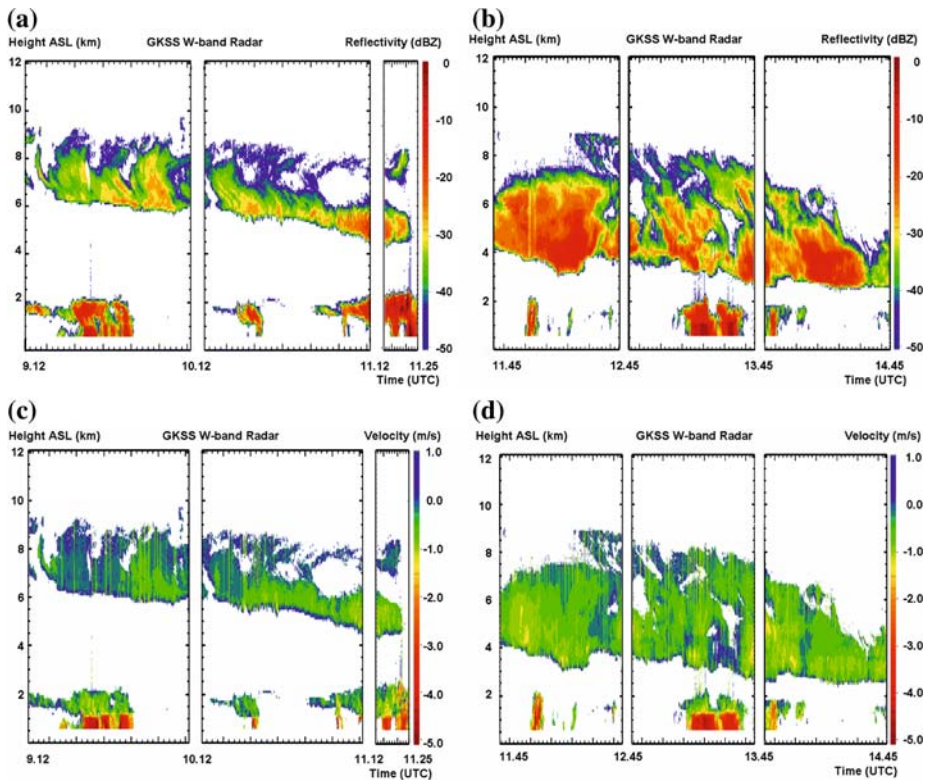| Instruments					
Cloud Doppler radar miracle (GKSS)	Wavelength frequency	Energy/pulse	Pulse frequency	Vertical resolution	Field of view
	3.2 mm 94.9 GHz	1.5 KW	50 Hz–80 kHz	28 m	3 mrad
PMS FSSP-100	Ranges of the particle sizes	2–47 microns			
OAP 2D2-C		25–800 microns			
OAP 2D2-P		200–6400 microns			

Fig. 1 Reflectivity (dBZ) measurements (**a**) and (**b**) and Doppler velocity (m/s) measurements (**c**) and (**d**) for 10 November 2000, as obtained from the GKSS W-band Radar during the experimental campaign

2.2 Large-scale weather conditions

During the day of interest (10 November 2000), a deep low pressure system extended from the surface to the upper troposphere and associated with frontal zone, was established over the North Atlantic (Figs. 2, 3). This synoptic pattern resulted in the development of a SW flow over the experimental site close to the ground (Fig. 2a). In the middle troposphere a westerly flow was persisted (Fig. 2b), while finally a strong northwesterly flow dominated

in the upper troposphere (Fig. 2c, d). The warm and moist air masses transferred from the Atlantic Ocean created a cloud system, which covered the western part of Europe, as it is illustrated in Fig. 4, and later extended eastwards. The observed cloud structure (low and middle-height clouds) was associated to the warm sector of the middle latitude cyclone as it reached to the western coast of France (Figs. 3 and 4).

3 Model description and configuration

3.1 Model description

The regional atmospheric modeling system (RAMS) is a well-known numerical model initially developed at Colorado State University and Aster Division of Mission Research Inc. (http://www.atmet.com) for research purposes (Pielke et al. [3]). It is most frequently used to simulate atmospheric phenomena on the mesoscale (horizontal scales from 2 to 2000 km) and for various applications. Cotton et al. [26] provided an overview of the model current status focusing on new developments in the RAMS physics and computational algorithms since 1992. The physical package of the model describes various atmospheric effects, including also the microphysical processes in clouds.

The horizontal and vertical grid spacing configured in the model determine the spatial scales of prognostic field variables that can be explicitly resolved and those which cannot. For momentum and conservative scalars Reynolds averaging of the prognostic differential equations for momentum and conservative scalars is performed in order to partition advective transport into resolved and unresolved components. RAMS parameterizes the unresolved transport by the use K-theory. The covariances are evaluated as the product of an eddy mixing coefficient and the gradient of the transported quantity. For scalars, this parameterization takes the form:

$$\overline{u_i'\phi'} = -K_{hi}\frac{\partial \phi}{\partial x_i} \tag{1}$$

where K_{hi} is the eddy mixing coefficient for scalars which applies to the i-direction. This coefficient is never negative, which means that the parameterized eddy fluxes are always down-gradient. For velocity components, if the horizontal grid spacing is comparable to the vertical spacing, the Reynolds stresses are evaluated from:

$$\overline{u_i'u_j'} = -K_{mi}\left(\frac{\partial u_i}{\partial x_j} + \frac{\partial u_j}{\partial x_i}\right) \tag{2}$$

which applies to the i-direction for i and $j = [1,2,3]$, where K_{mi} is the eddy mixing coefficient for momentum. In this case, it is assumed that $K_{mi} = K_{mj}$, and therefore, $\overline{u_i'u_j'} = \overline{u_j'u_i'}$. For coarse horizontal grid spacing the expression (2) is applied only in horizontal directions by restricting i and j to $[1,2]$. Whenever i and/or j is 3 the following expression is used:

$$\overline{u_i'u_j'} = -K_{mi}\left(\frac{\partial u_i}{\partial x_j}\right) \tag{3}$$

There are four basic options for computing K_{mi} and K_{hi}. Two of these are purely local schemes and based on the Smagorinsky [27] scheme which include corrections for the influence of Brunt–Vaisala frequency (Hill [28]) and Richardson number (Lilly [29]). The other two options diagnose mixing coefficients from a parameterized subgrid-scale turbulent kinetic energy (TKE) which is prognosed in the model. Although the diagnosis is
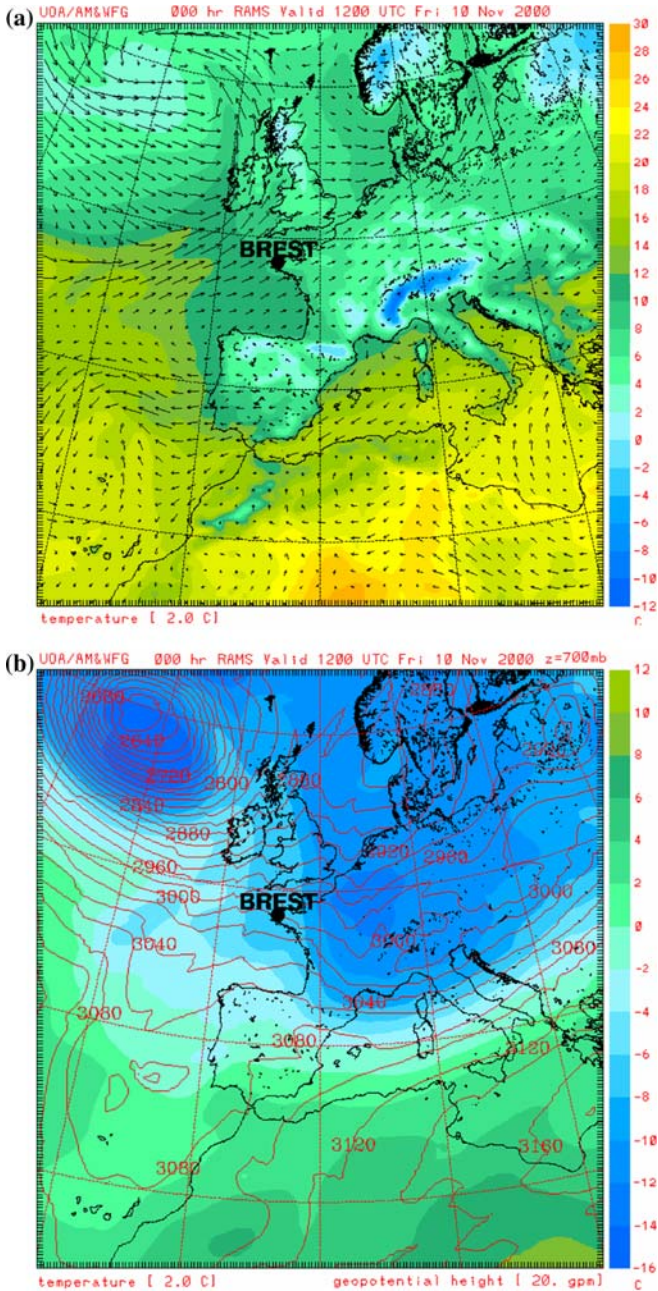
Fig. 2 ECMWF analysis data valid at 12:00 UTC, 10 November 2000: (**a**) Wind field (*arrows*) and temperature in color (at 2°C intervals) at the first model level above the ground; (**b**) Geopotential height in contours (at 20 gpm intervals) and temperature field in color (at 2°C intervals) at the 700 hPa isobaric surface, (**c**) Geopotential height in contours (at 40 gpm intervals) and temperature field in color (at 2°C intervals) at the 500 hPa isobaric surface and (**d**) Geopotential height in contours (at 40 gpm intervals) and temperature field in color (at 2°C intervals) at the 300 hPa isobaric surface
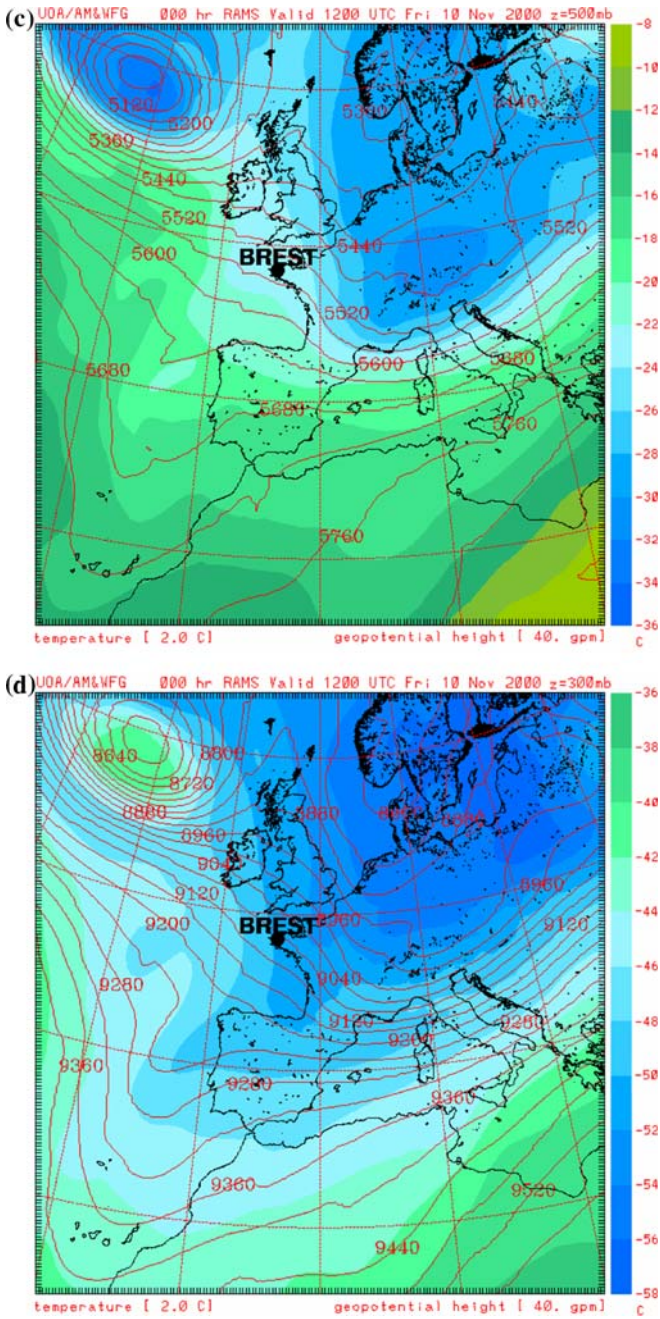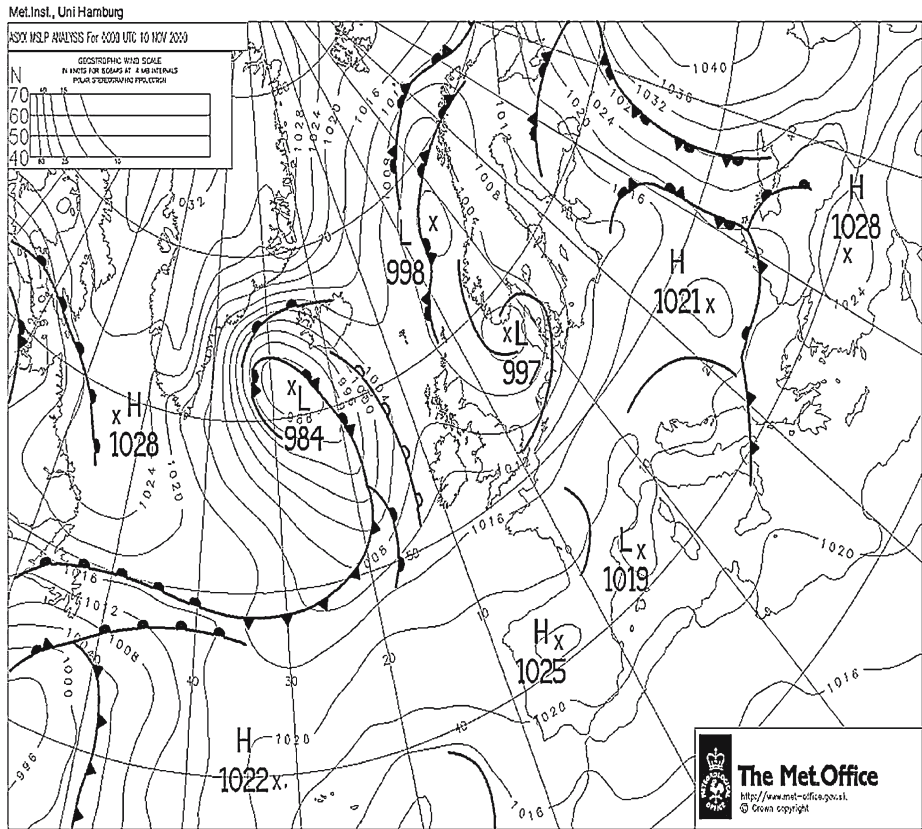
Fig. 2 continued

Fig. 3 Surface pressure analysis field (at 4 hPa intervals) from UK MetOffice, valid on 12:00 UTC 10 November 2000

based on the local curred value of TKE, these schemes are regarded as non-local because the TKE can be generated elsewhere in the domain and transported to new locations.

The cloud microphysics scheme in RAMS (Walko et al. [30]; Harrington et al. [31]; Meyers et al. [32]) predicts the mixing ratio and number concentration of rain, pristine ice crystals, snow, aggregates, graupel and hail. The liquid water is categorized into cloud and rain, which may be super-cooled, while ice is categorized into pristine ice, which is pure vapor-grown crystals, and snow, which is larger vapor-grown crystals and crystals that undergo moderate riming. Aggregates remain as a separate category and are formed by collision and coalescence of pristine ice, snow, and/or other aggregates, while it is allowed to retain their identity with moderate amounts of riming. Graupel is mixed-phase, spherical in shape and low-density particle, which are formed by heavy riming and/or partial melting of pristine ice, snow and aggregates. Graupel can carry a small percentage of liquid. If this percentage is exceeded, the graupel is re-categorized as hail, which is an additional category that represents spherical in shape and high-density frozen particles, such as frozen raindrops and hailstones. It is assumed that the hail particles are formed from freezing of raindrops or by riming or partial melting of graupel. All the categories can fall on to the Earth, with the exception of cloud droplets and pristine ice, which are assumed to be too small to fall.
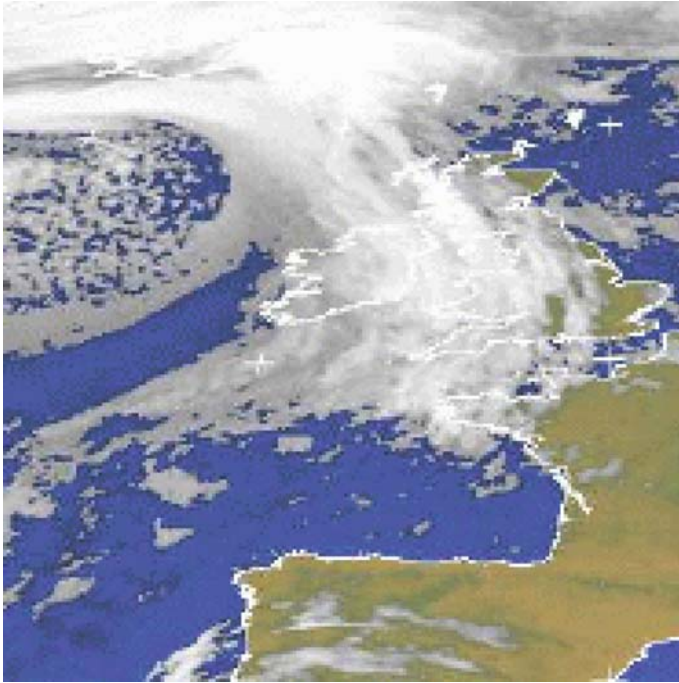
Fig. 4 Meteosat IR image at 12:00 UTC, 10 November 2000 (from Pelon et al. 2001)

The general gamma distribution (Flatau et al. [33], Verlinde et al. [34]) is the basis function used for hydrometeor size in each category:

$$n(D) = \frac{N_t}{\Gamma(\nu)} \left(\frac{D}{D_n} \right)^{\nu-1} \frac{1}{D_n} \exp\left(-\frac{D}{D_n} \right) \tag{4}$$

where, $n(D)$ is the number of particles of diameter D, N_t is the total number of particles, ν is the shape parameter, and D_n some characteristic diameter of the distribution. The Marshall–Palmer (exponential) distribution function is special case of this generalized function. When two-moments of a hydrometeor class is predicted, all that is needed to completely specify the distribution function given by (4) is the specification of ν. Except for few cases where observations can be used to specify ν, its value is chosen by trial and error or altered in sensitivity experiments.

Additional features include: use of stochastic collection for number concentration tendency, breakup of rain droplets formulated into the collection efficiency, diagnosis of ice crystal habit dependent on temperature and saturation, evaporation and melting of each species and more complex shedding formulations taking into account the amount of water mass on the coalesced hydrometeor. The prognostic equation for the various hydrometeors, except for the cloud water and vapor is:

$$\frac{\partial r}{\partial t} = ADV(r) + TURB(r) + SOURCE(r) - SINK(r) + SED(r), \tag{5}$$

where, *ADV(r)* and *TURB(r)* represent the advective and turbulent transport of species *r*. The *SOURCE(r)* and *SINK(r)* terms represent the possible generation or loss of the species *r* by

Table 2 Summary of the horizontal and vertical grid configuration parameters, for the three RAMS grids. The model parameters include the number of grid points in the three directions (nx, ny, nz), the horizontal grid spacing (dx,dy) and the minimum and maximum vertical resolutions (dzmin and dzmax)

Grid	nx	ny	nz	dx, dy (km)	dzmin (m)	dzmax (m)
1	64	92	45	50	46	1000
2	122	157	45	10	46	1000
3	94	106	45	2.5	46	1000

microphysical processes, while the *SED(r)* accounts for local loss or gain of species *r* due to gravitational sedimentation.

Nucleation results from two primary processes: (a) a combination of vapor deposition and condensation-freezing mechanism for which the amount of activated nuclei is derived from the amount of supersaturation with respect to ice (Meyers et al. [35]) and (b) contact nucleation for which the number of potential nuclei is derived from an observed temperature dependence. At colder temperatures such as found in cirrus clouds, primary nucleation by homogeneous freezing of supercooled cloud drops and haze particles have been introduced (DeMott [36]).

The secondary ice particle production model in RAMS is based on Mossop [37]. In S.I. units, the formula is:

$$N_i = 9\exp(-10) \times B \times N_{24} \times (N_{13})^{0.93} \tag{6}$$

where N_i is the number of ice particles produced per second, N_{24} is the number of cloud droplets larger than $24\,\mu$m in diameter that are collected by ice each second, N_{13} is the number of cloud droplets smaller than $13\,\mu$m in diameter that are collected by ice each second. The factor B increases linearly from 0 to 1 as ice temperature T increases from -8 to $-5°$C, B decreases linearly from 1 to 0 as T increases from -5 to $3°$C and B is zero at other ice temperatures.

3.2 Model configuration

For the case studied RAMS model ran on three nested grids (Fig. 5). A horizontal grid spacing of 50, 10 and 2.5 km and a stretched vertical coordinate (45 levels) from 46 m near the ground up to 18.3 km at the top of the domain have been chosen. Due to the importance of the model domain characteristics (e.g., domain size, vertical layering), the vertical structure of the RAMS grids was adequately specified for a satisfactory representation of the atmospheric layering. More vertical layers are always desirable in model simulations, especially for studies focusing on cloud formation processes. Thus, several sensitivity tests with varying numbers of vertical layers, from 30 to 65, were performed for domain selection, grid resolution and vertical structure. However, the computational cost is still considerable for a large number of vertical layers. Therefore, a number of vertical layers between 40 and 50 are considered as adequate for a good representation of the vertical tropospheric structure with reasonable computational load. Concerning the horizontal grid structure, several tests have been performed in order to find configurations in which the travelling time from inflow to the area of interest would be lower than the model simulation period. A summary of the horizontal and vertical grid parameters is provided in Table 2.
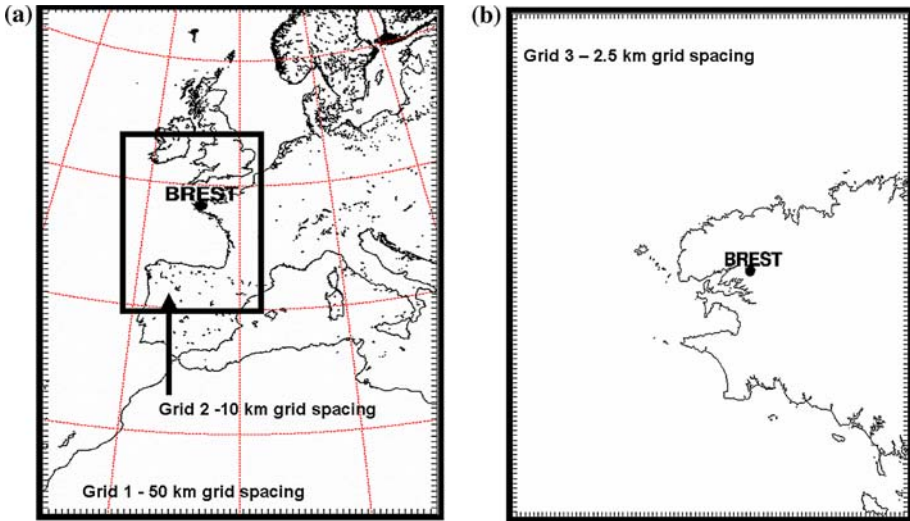
Fig. 5 (**a**) Area covered by the first model grid (50 km horizontal grid spacing) and the second model grid (10 km horizontal grid spacing) and (**b**) area covered by the third model grind (2.5 km horizontal grid spacing)

Sensitivity analysis of the model configuration was also performed in relation to the initialization time of the simulation. As expected, it appears that cloud formation at the local scale is affected by the initialization time during the prime stages of the model simulation. This is mainly due to the influence of the initial conditions imposed. For this reason, in order to exclude any possible influence owed to the initial conditions, the model was initialized 24 h before the day of interest (10 November 2000) and the simulation started at 00:00 UTC 9 November 2000 with a time step of 60 s.

The physical parameterization schemes used in the model simulations includes: (a) the Klemp/Wilhelmson (Klemp and Wilhelmson [38]) radiative type lateral boundary conditions to the outer grid, (b) the two-moment microphysics scheme described in Sect. 3.1, (c) the Kain–Fritsch cumulus parameterization scheme for the convective dynamics in the outer grid (Kain and Fritsch [1,39]), (d) the Chen and Cotton [40] radiation scheme and (e) a 10-layer soil/vegetation/snow parameterization (LEAF-2/.Walko et al. [41]).

For initial and boundary conditions the ECMWF (European Center of Medium Range Weather Forecasts) $0.5° \times 0.5°$ gridded objective analysis fields were used, which was enhanced with soundings and surface observations (from ECMWF) retrieved in 6-h intervals. For the water body mean-monthly $1°$ gridded sea-surface temperature (SST) data set was used, whereas the topography derived from $30''$ resolution terrain data (USGS data set). Finally, gridded vegetation type data (USGS data set) of $30''$ resolution was used to synthesize vegetation cover at each grid cell.

4 Results from model simulation

During the 10 November 2000 CARL experiment the cloud system covered initially the western part of Europe and later extended eastwards, as it is illustrated in Fig. 4 (Meteosat IR image) and Fig. 6 (cloud fraction prepared from the model simulation).
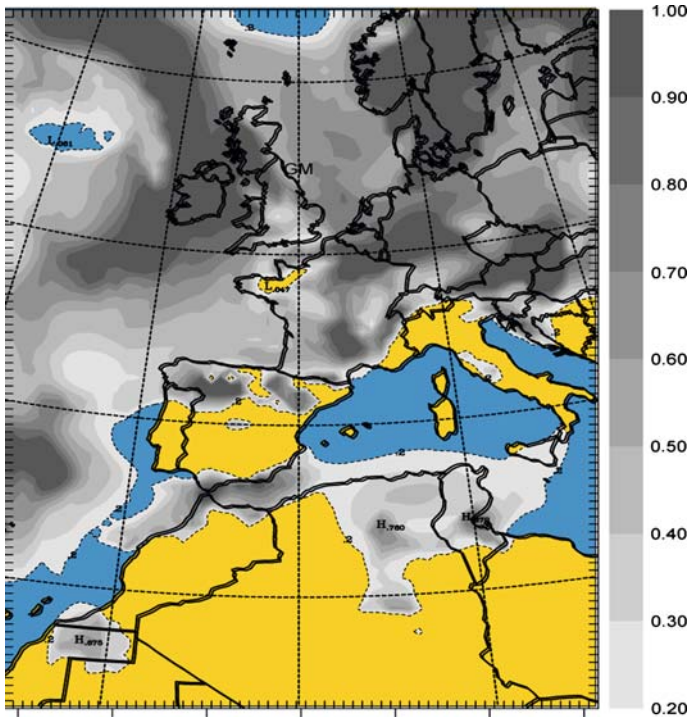
Fig. 6 Cloud fraction for the outer model grid, as simulated by the RAMS model, valid at 12:00 UTC, 10 November 2000

The discussion of the model results is mainly focused on the explicitly resolved microphysical parameters and specifically on the ice/liquid water content (IWC/LWC), the number concentration (N_t) and the size of liquid and frozen water forms, namely rain drops, cloud droplets, pristine ice, snow, aggregates, graupel and hail. Time/height plots were prepared and shown below, to understand the vertical structure of the cloud microphysical processes, as well as to compare observations with model output. For the preparation of these plots, vertical profiles over the grid point which coincides with the location of the experimental site in Brest (Fig. 5) were extracted from the 3D fields at intervals of 5 min for a 9-h time period (between 6:00 and 15:00 UTC). Additional cross-section of air temperature is also provided. A lower threshold of $0.003\,\text{g/m}^3$ was selected for IWC and LWC for the two cloud layer's identification. Guan et al. [15] have performed sensitivity tests, which indicated that the use of thresholds of up to $0.01\,\text{g/m}^3$ produced only small changes in the verification statistics.

Emphasis was given on the sensitivity of the model related to the shape parameter of *gamma* distribution in the cloud microphysics module. It has been reported that increased values of the shape parameter affect the microphysical characteristics of the precipitation process (Krichak and Levin [42]). The sensitivity tests, performed for the present study, showed that the microphysical structure of the cloud system is sensitive to the selection of the ν-shape parameter. In cases where the shape parameter was chosen to be greater than 1 (the same value used for all species), the model simulations gave less realistic results of the cloud microphysical structure and showed an increased development of large size hydrometeors with corresponding reduction of small and medium size water species, while
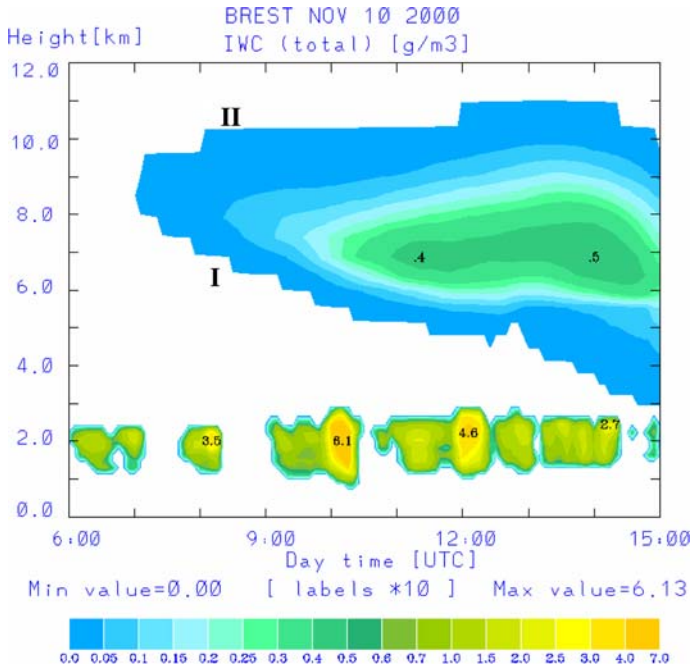
Fig. 7 Time/height cross-sections over the experimental site of simulated total ice water content (g/m³ multiplied by 10)

the configuration with $\nu = 1$ for all species lead to results that are closer to the observational data, especially at the lower cloud layer. The results of this simulation are reported and discussed below. Another important input parameter is the concentration of the initially activated cloud droplets. This concentration was chosen to be equal to $500 \, \text{cm}^{-3}$, which is a climatologically derived value used in simulations for similar cases.

4.1 Microphysical characteristics of the cloud formation

According to the model results, a low cloud formation from near-surface up to about 2.5 km height was evident from the beginning of the period considered (10 November). This formation, which is referred to as I in Fig. 7, was consisted of mixed phase hydrometeors (ice particles co-exist with liquid water species). This mixed-phased layer was approximately 1500 m thick and was at most broken during the simulation period. After about 06:00 UTC an upper layer (marked with II in Fig. 7) of frozen water species started to be formed. During the day, this layer extended downwards to 3 km ASL at about 15:00 UTC and consisted exclusively of pristine ice and snow. Figure 8 provides mean modeled ice concentrations and the corresponding standard deviations per size range of ice particles. As it is illustrated in this figure the main body of the ice species has diameters of less than 100 microns. The higher values of the standard deviations, which are shown in Fig. 8a, suggest that a remarkable temporal variability within the lower cloud formation is obtained. The same conclusion is also supported by Fig. 7 showing the temporal variation of total ice IWC.

The simulation showed pristine ice crystals in the lower (I) cloud formation. The incloud model calculated concentrations were of the order of $0.05–200.01^{-1}$, with a maximum point

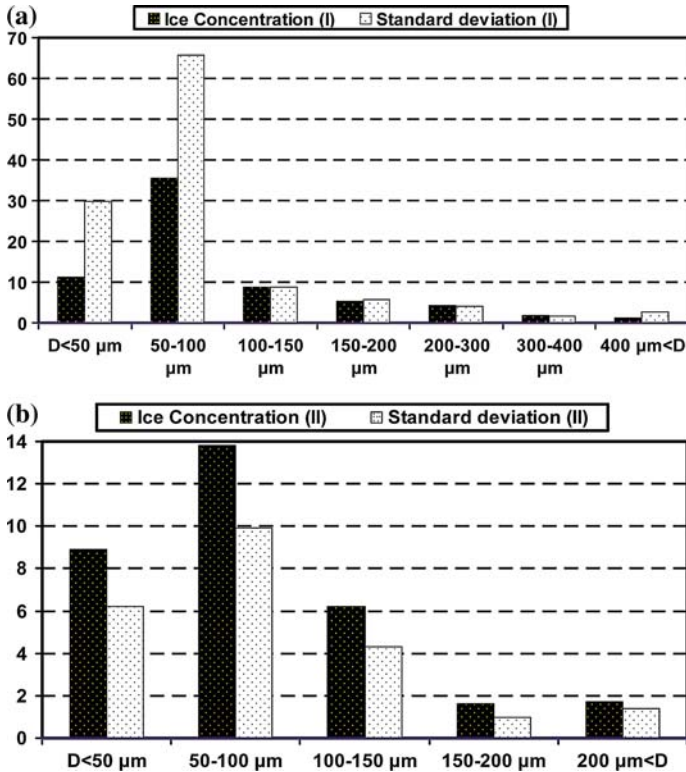**Fig. 8** (**a**) Mean concentrations (l^{-1}) and corresponding standard deviations per size range of total ice based on the model simulation within the lower cloud formation (I) and (**b**) the same as (**a**), but for the upper cloud formation (II)

value of 587.3 l^{-1} (Table 5) and an overall mean for this cloud layer of 52.1 l^{-1}. The highest concentrations of small pristine ice (diameters smaller than 50 microns) were developed near the top of this cloud layer in short time periods at about 7:00, 8:00, 13:30 and 14:20 UTC, as shown in Fig. 9a. The corresponding maximum point values for these periods were 186.1 l^{-1}, 281.3 l^{-1}, 536.2 l^{-1} and 587.3 l^{-1}, respectively. At this stage, the ice particles might be produced by secondary ice formation mechanism through rime-splintering (see Sect. 3.1). According to the literature (e.g., Houze, Jr. [43]) when the top of mixed-phase stratocumulus clouds extends to heights above the $-6°C$ level, high concentrations of ice particles (rising from 1 to 1000 per liter) might be produced within the cloud layer in less than 10 min. This seems to be confirmed in these case study simulations. According to the model results, the top of the lower cloud formation was up to $-8°C$ level, as it is shown in Fig. 9b. Pristine ice formation is also found in the upper cloud layer (II), with concentrations ranged from about 0.05 to 30 l^{-1} and an overall mean for this cloud layer of 17.2 l^{-1}. The maximum value (34.2 l^{-1}) was calculated near the top of the layer at about 13:00 UTC (Fig. 9a). Since pristine ice number concentration (N_t) increases with height, it can be concluded that primary ice formation is likely to occur near the top boundary of the upper cloud. The IWC values for the lower cloud layer (I) were up to 0.034 g/m^3, with the maximum point value being simulated near the top of the cloud at about 14:20 UTC (Table 5). The IWC values of the upper cloud formation (II) were found an order of magnitude less than those of the lower cloud (I). Details on the IWC of pristine ice are also provided in Table 3. Since for the majority of the
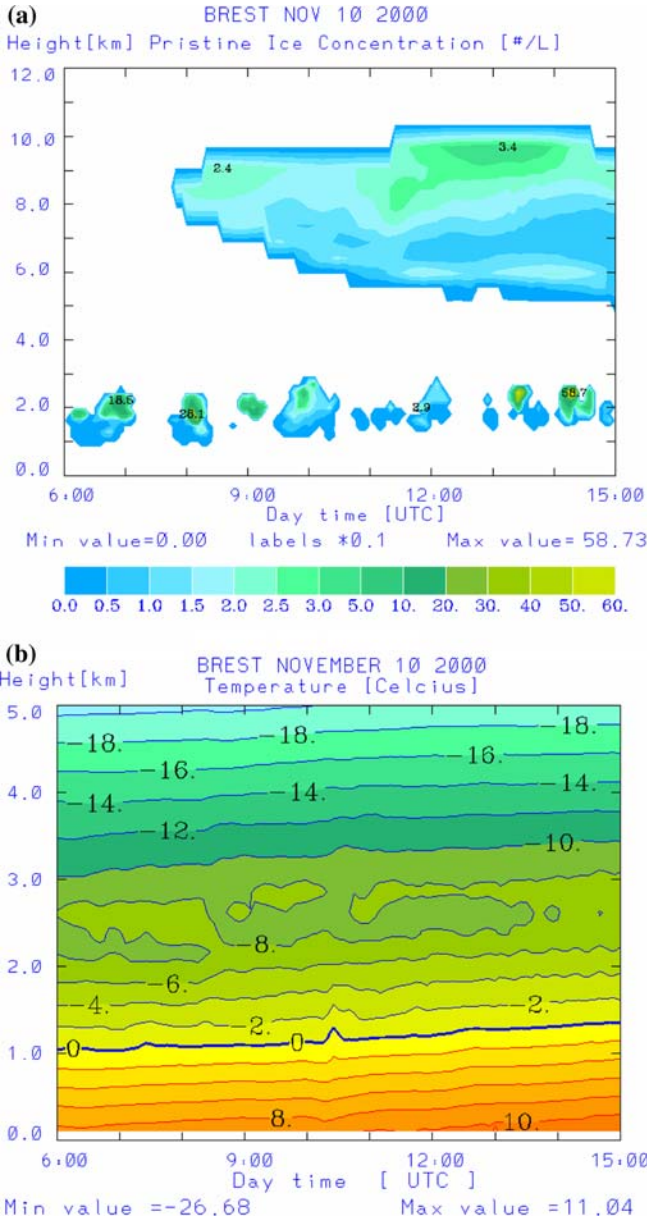
Fig. 9 Time/height cross-sections over the experimental site of: (**a**) simulated concentration of pristine ice particles (l^{-1} multiplied by 0.1), (**b**) simulated air temperature within the lower 5 km of the atmosphere (in Celcius), (**c**) simulated snow concentration (l^{-1}) and (**d**) simulated IWC of aggregates (g/m^3 multiplied by 10) within the lower cloud formation

model calculated pristine ice the mean size appears to be less than 100 microns in diameter (mean concentration 45.91^{-1}), the average diameter of these particles was calculated equal to $67.55\,\mu$m with corresponding standard deviation equal to $64.04\,\mu$m (Table 4).

At the same time period, the majority of the model-calculated snow crystals has been developed in the lower (I) cloud layer. The model calculated snow concentrations were of
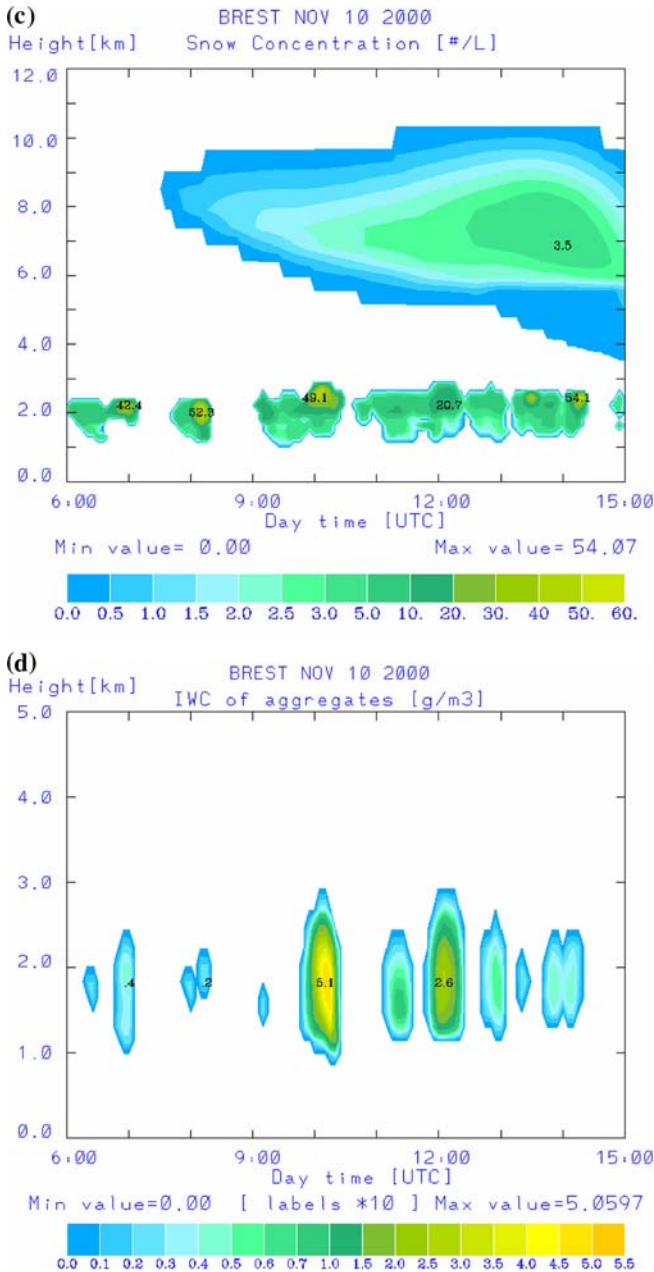
Fig. 9 continued

the order of 0.05–50.0 l^{-1}, with a maximum point value of 54.1 l^{-1} near the top boundary of the cloud (Fig. 9c, Table 5). An overall mean for this cloud layer was of 12.1 l^{-1}, while snow formation was also found in the upper (II) cloud formation, as it is shown in Fig. 9c. For this upper layer, the number concentration values were found an order of magnitude less than those of the lower cloud (I) reaching a maximum point value of 3.5 l^{-1}. In the

Table 3 Highest and Average IWC (g/m³) values (with corresponding standard deviation) of pristine ice, snow and aggregates, based on the model simulation (a lower limit of 3.0×10^{-3} g/m³ has been assumed)

Ice forms	Cloud layers	Highest IWC	Average IWC	Stdev
Pristine ice	Lower (I)	0.034	0.00074	0.0029
	Upper (II)	0.004	0.00014	0.0003
Snow	Lower (I)	0.332	0.0381	0.0569
	Upper (II)	0.047	0.0025	0.0085
Aggregates	Lower (I)	0.506	0.0198	0.0559

Table 4 Additional information on the size of pristine ice, snow and aggregates based on the model simulation

Ice forms	Average diameter (μm)	Standard deviation (μm)
Pristine ice	67.55	64.04
Snow	173.31	76.65
Aggregates	690.09	233.19

Table 5 Summary of the highest IWC and number concentration values of the various water forms within the lower cloud, as simulated by the model

Water forms	Values	Time (UTC)	Height(m)
Highest IWC of pristine ice (g/m³)	0.034	14:20	2323
Highest number concentration of pristine ice (l^{-1})	587.3	14:20	2323
Highest IWC of snow (g/m³)	0.332	10:10	2323
Highest number concentration of snow (l^{-1})	54.1	14:20	2323
Highest IWC of aggregates (g/m³)	0.51	10:15	1696
Highest number concentration of aggregates (l^{-1})	18.9	10:15	1696
Highest IWC of graupel (g/m³)	0.077	10:15	868
Highest number concentration of graupel (l^{-1})	2.70	10:10,14:35	1014, 2323
Highest IWC of hail (g/m³)	0.021	10:15	729
Highest number concentration of hail (l^{-1})	0.776	10:10	868
Highest LWC of rain (g/m³)	0.079	10:20	475
Highest number concentration of rain (l^{-1})	13.6	14:50	2323
Highest LWC of cloud particles (g/m³)	1.0	14:50	2323

model microphysics scheme the snow crystals are formed from pristine ice through vapor deposition. This is the reason why snow was mainly reproduced by the model in the vicinity of cloud layers characterized by high values of pristine ice number concentration (Fig. 9a). The modeled snow crystals exhibit a size distribution characterized by a decreasing concentration towards the large end of the size spectrum. The mean size of snow crystals appears to be about 100–300 microns in diameter. The IWC was up to 0.332 g/m³ within the lower cloud layer (Table 5), while within the upper cloud the IWC reached 0.0471 g/m³, as summarized in Table 3. Additional information concerning the size of snow crystals is given in Table 4.

The falling snow crystals of different sizes grow rapidly to form aggregates. This growth is certainly associated with a reduction in the number concentration of ice particles in these layers. Aggregation produces larger ice particles mainly within a 1 km layer above the 0°C level in the lower (I) cloud formation, with maximum IWC values of $0.51\,\text{g/m}^3$ at 10:15 UTC (Fig. 9d and Tables 3, 5) and maximum concentration of about 19 particles per liter of air (Table 5). The average diameter was calculated equal to $690.09\,\mu\text{m}$ with corresponding standard deviation equal to $233.19\,\mu\text{m}$, as shown in Table 4.

Due to the fact that the surfaces of ice crystals become sticky at temperatures in the vicinity of -5°C, the probability of adhesion of colliding ice particles increases as temperature increases and hence the particle sizes increase sharply at temperatures above -5°C (Walko et al. [30], Houze, A. R., Jr. [43]). For this reason the maximum number concentration and IWC of aggregates were reproduced by the model at locations characterized by temperatures close to -5°C (1.8 km ASL, see Fig. 9b). According to the model microphysics scheme these particles could be reproduced by the interaction between the ice crystals themselves or by high riming (Walko et al. [30]). The latter process requires high values of LWC and large crystal sizes, namely diameter (D) $> 300\,\mu\text{m}$ (Hobbs et al. [44]). This seems to be confirmed during the model simulations. As it is shown in Figs. 9d and 10d, locations within the cloud characterized by high IWC of aggregates, coincide spatiotemporally with high values of LWC.

According to model results, negligible quantities of mixed phase water substances (graupel and hail) were reproduced by the model within the lower cloud layer (I) in the vicinity of the zero degree level (it is located at around 1 km ASL Fig. 9b), which indicates the transition from ice to liquid phase. These groups of particles are treated as transitional particles between the ice and liquid phases in the RAMS microphysics scheme. Partial melting of snow and aggregates cause some of their mass to be converted into graupel, and partial melting of graupel causes some of its mass to be converted into hail. These hail particles are not traditional hail and could happen in any cloud (Walko et al. [30]). They are not the result of strong updraft activity, since such an activity was not observed in this case (not shown). According to the literature (Cotton and Anthes [45], Pruppacher and Klett [46]), such formations can originate under certain conditions, since there is some indication that aggregates of ice crystals can serve as embryos for the development of graupel particles. The maximum number concentration of graupel and hail was 2.68 and $0.776 1^{-1}$ (see Table 5 and Fig. 10a, b), while the maximum IWC values were 0.077 and $0.021\,\text{g/m}^3$, respectively (Table 5).

Aggregation concentrates condensate into large particles, which, upon melting, become large falling drops. The appearance of water in liquid phase (Figs. 10c, d) varied in height and time during the simulation within a layer of about 2.5 km thick. The model results showed the base of this layer to be near the ground level, while its top was approximately 1 km above the freezing level. The plots (Figs. 10c, d) show a tendency for LWC to increase with height. Large amounts of cloud droplet mass (LWC) were found at the top of this layer ($1.0\,\text{g/m}^3$), while the higher number concentration of rain drops (13.61^{-1}) was reproduced by the model at the top of this cloud layer (at about 15:00 UTC). It is suggested that liquid dominates the cloud top despite depositional growth of ice crystals because the ice crystals near the cloud top were small. Several prior works have observed mixed phase cloud layers in which LWC increases with height in midlevel clouds (e.g., Hobbs et al. [44], Fleishauer et al. [47]). The same structure has also been obtained in numerical simulations of arctic boundary layer stratus (Harrington et al. [9]).

The location of the higher number concentration of rain coincides spatiotemporaly with the higher concentrations of graupel (with a time shifting of about 15 min, see Fig. 10a, Table 5) and also with the higher values of LWC of cloud droplets (Fig. 10d, Table 5).
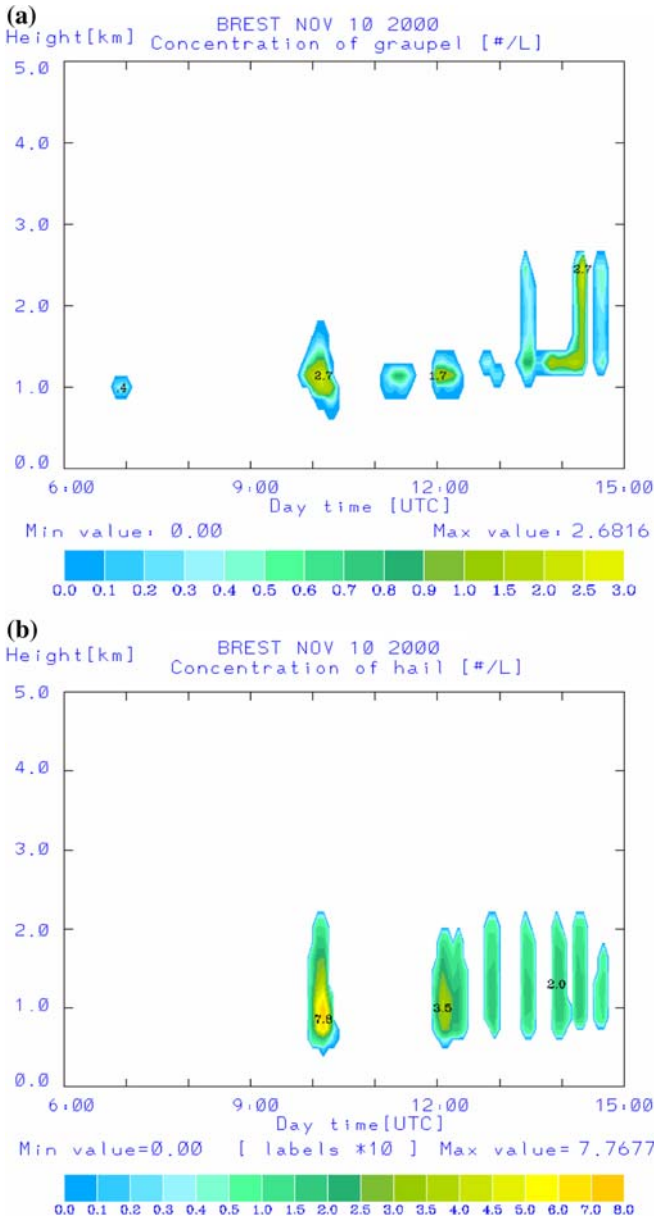
Fig. 10 Time/height cross-sections over the experimental site of simulated: (**a**) concentration of graupel (l^{-1}), (**b**) concentration of hail (l^{-1} multiplied by 10), (**c**) concentration of rain drops (l^{-1}) and (**d**) LWC (g/m^3) of cloud droplets

This implies that a part of the rain drops was produced by the melting of the mixed phase hydrometeors, while the other part of rain drops could be generated by the growth of the cloud droplets. According to the model results, rainfall, in low amounts, was evident during most of the period under study (see Fig. 10c), although there are periods with no rain reaching the ground. The modeled rainfall values were comparable to the measured ones, as shown in Table 6.
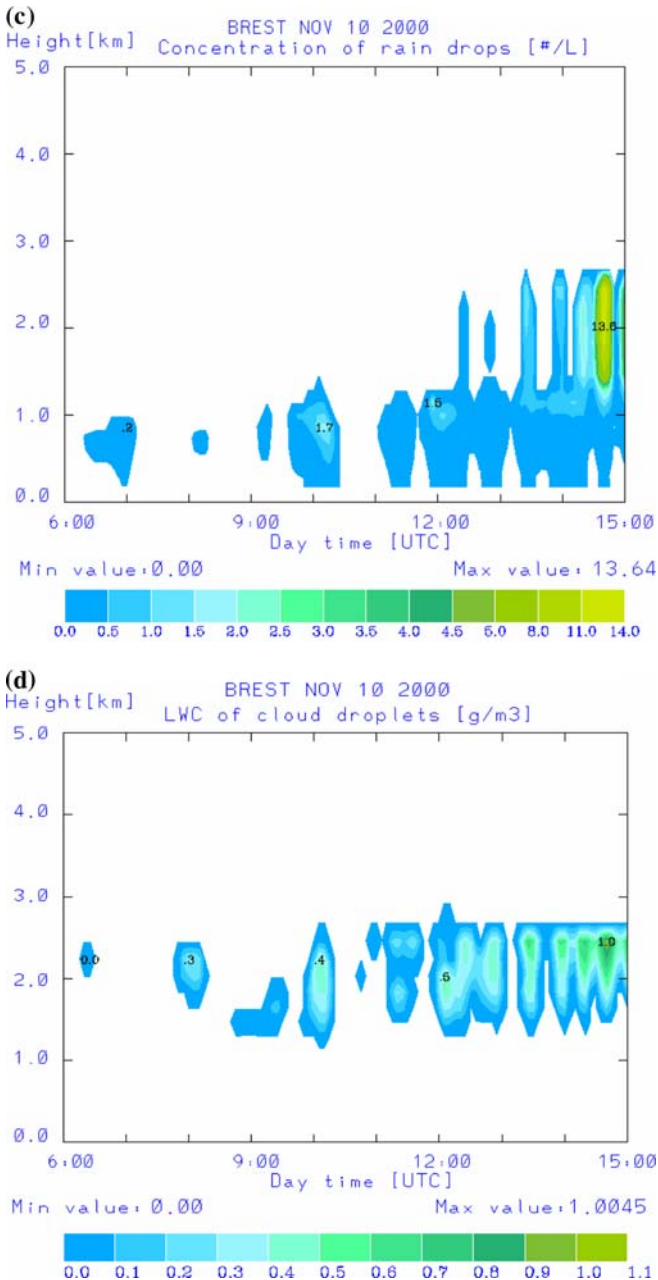
Fig. 10 continued

This case study illustrates an important feature of the multilayered systems. As it is shown in Table 5 and discussed previously, significant amounts of ice appear at the top of the lower cloud layer. This is in contrast to the mid- to lower- cloud maximum observed in the single-layer cases (e.g., Hobbs et al. [44], Harrington et al. [9]), which suggests that different mechanisms or processes may work for the single-layer clouds and multilayered systems. We

Table 6 Simulated rainfall values and rainfall observations over brest. The observational data are provided by the ECMWF

Time period (UTC)	00:00–06:00	06:00–12:00	12:00–18:00
Modeled values (mm/6 h)	0.83	0.75	0.92
Measurements (mm/6 h)	0.6	1.0	1.0

discuss the hypothesis that the ice at the top of the lower cloud formation might have been introduced, at least partially, by a seeder-feeder mechanism. The seeder-feeder mechanism is a process in which ice particles form in the cloud above and sediment into clouds below (e.g., Houze, Jr. [43]). There are many prior works where the seeding process in multilayered clouds is noted (e.g., Hobbs et al. [44], Lawson et al. [48]).

The main evidence for a seeder-feeder process in the multilayer case in this study is the detection of some ice particles between the layers by the 2D2-C and 2D-P probes, as well as direct observations (by the GKSS radar) of ice particles falling from the upper cloud layer into the lowest layer (Figs. 1a, b). Low amounts of ice particles have also been calculated by the model between the two cloud layers (Figs. 11a, b), especially in the afternoon hours, as it is represented in Fig. 11a.

The evidence in favor of the seeder-feeder mechanism is balanced by the evidence that the effect was weak. In particular, the number of ice particles that was directly observed and modeled between the cloud layers was probably too small to account for all the ice in the top of the lower cloud layer. This is why we cannot make general statements about the vertical structure of ice or the efficacy of the seeder-feeder mechanism in multilayer cloud systems.

4.2 Comparison of the model results with observations

During the day of interest, 10 November 2000, the radar detected two main cloud layers (Figs. 1, 12a and b). One layer was obtained at heights below 2 km, while the second one extended between 3 and 9 km. As it is simulated by the model and confirmed by the radar detections, the upper cloud layer was characterized by small temporal variability. The opposite was found for the lower cloud formation, where the temporal variability was high in both ice (Fig. 7, left part of Fig. 12a and left corner on the bottom of Fig. 12b) and liquid phase hydrometeors (Figs. 10c, d). As it is shown in Fig. 12a, the maxima of the modeled number concentration of total ice compare well in time and height with the radar detections. For the lower cloud formation, precipitation was observed below the 1.2 km altitude. This was captured by the radar with a melting layer suggesting the transition from mixed ice/water particles through to rain. The radar detected an increase in the particle fall velocities at the atmospheric levels below this height (top of Fig. 12b). This could be explained by the change in the particle shape from irregular ice crystals to tear-like water drops, which leads to a decrease in the drag of the particle. The maxima of the fall velocities fit fairly well in time with the maxima of the model simulated precipitation rate (right corner on the bottom of Fig. 12b). The model results showed that the lower cloud layers with water in liquid phase (Figs. 10c, d) were around and below the zero degree isotherm, which was slightly increasing from 1 to 1.2 km during the day (Fig. 9b). This is in good agreement with the radar detections (top of Fig. 12b) and radiosonde data (Fig. 14a). The observed (and simulated) altitude of the zero degree isotherm, which makes ice occurrence possible in the low level clouds, suggests that the water in liquid phase (Figs. 10c, d) not only was the result of warm cloud formation
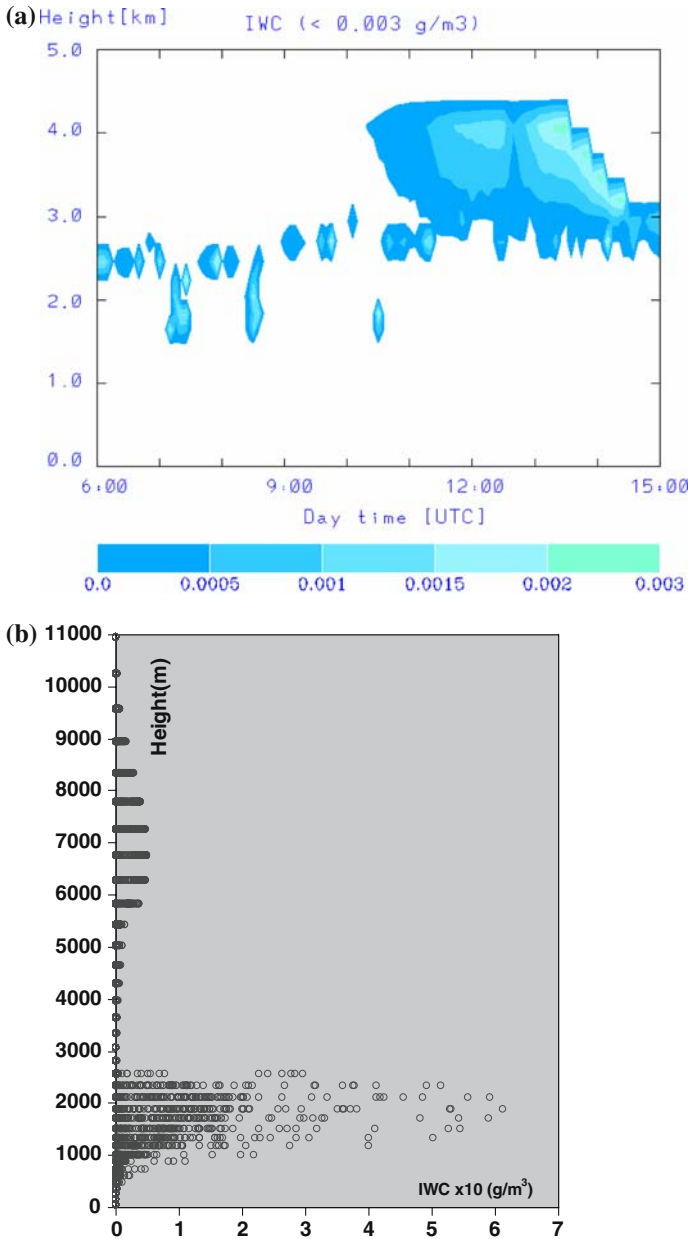
Fig. 11 (**a**) Time/height cross-section over the experimental site of simulated total IWC (g/m^3) between the two cloud layers. An upper limit of 0.003 g/m^3 has been selected and (**b**) Vertical profile of the simulated by the model total ice water content (g/m^3 × 10)

mechanisms, but it was also produced by the melting of frozen water substances. Furthermore, it can also be noted that the pattern of the temporal distribution of ice mass (total IWC) near the top of the lower (I) cloud layer (left corner on the bottom of Fig. 12b) is similar to the pattern of the precipitation rate on the ground (right corner on the bottom of Fig. 12b).
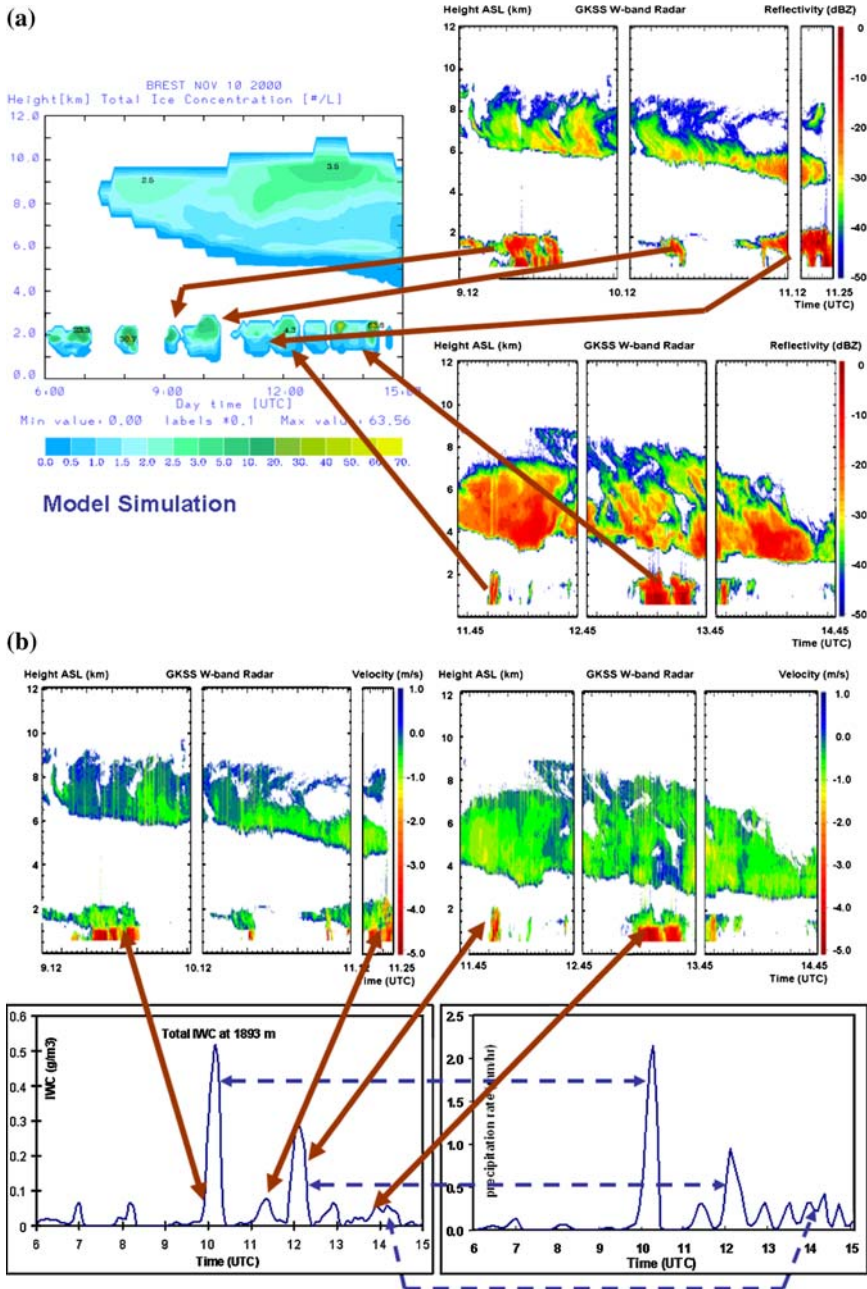
Fig. 12 (**a**) Time/height plot of total ice number concentration (l^{-1}) based on the model data, which extracted over the corresponding to Brest grid point (left part of the plot) and Radar reflectivity measurements in dBZ (right part of the plot) for 10 November 2000, as obtained from the GKSS W-band Radar during the experimental campaign, and (**b**) Doppler velocity (m/s) for 10 November 2000, as obtained from the GKSS W-band Radar during the experimental campaign (top of the Figure), simulated IWC (g/m^3) in the vicinity of the top of the lower cloud layer (1893 m) over the corresponding to the experimental site grid point (left corner on the bottom of the plot) and simulated precipitation rate (in mm/h–right corner on the bottom of the plot) at the same grid point for 9-hourly period
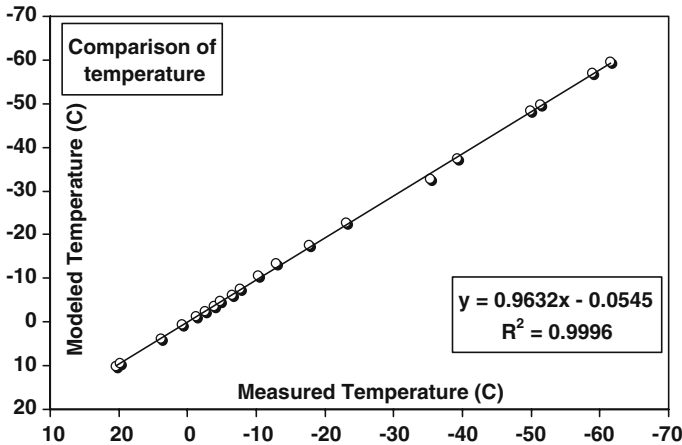
Fig. 13 RAMS simulated temperature versus sounding values taken over the experimental site in Brest. The model values are linearly interpolated form the model levels to the sounding levels. The solid curve represents the least square regression line. The least square regression line equation and the square of the linear correlation coefficient (R^2) are also shown

Figure 13 provides a comparison of model simulated temperature field with temperature sounding measurements taken over the experimental site, with the corresponding linear correlation coefficient. The model values are linearly interpolated from the model levels to the radiosonde levels. As it is shown, the simulated temperature compares fairly well with the measured temperature, since the average difference between the two curves is about 0.5°C.

Studies of stratocumulus clouds often reveal substantial temperature inversions at cloud top. For example, Albrecht et al. [49] showed temperature inversions as strong as 7–8°C in their analysis of marine stratocumulus off the coast of California taken during FIRE project, while Bretherton and Pincus [50] observed 2–4°C inversions in temperature soundings from the Atlantic Stratocumulus Transition Experiment. In contrast, the CARL measurements showed an almost linear decrease of temperature with height through the cloud (Fig. 14a), while the vertical profile based on the model calculated temperature field shows a weak temperature inversion of 0.5–1.0°C over the top of the lower cloud layer (Figs. 9b and 14a), which corresponds to the location of the model calculated LWC maximum (Fig. 10d). Our interpretation is that the cloud studied did not have strong inversion because of the fact that: (a) the clouds were strongly influenced by surface fluxes of energy due to the air flow coming from over the ocean onto the land. These fluxes may have driven boundary layer eddies that could lead to a weaker inversion; (b) no strong inversions were present when the cloud was formed; or (c) the cloud did not persist long enough to allow internal dynamic and thermodynamic processes to generate such inversions.

The model results were also compared with relative humidity (RH) measurements over the experimental site (Fig. 14b). In general the simulated RH compares fairly well with the measured one, regardless the fact that the model tends to overestimate RH except for the two narrow layers below 1 km and between 4.5 and 5.5 km respectively. Based on the relative humidity fields (model and measurements), clouds are expected to be formed in two distinct layers, namely at the boundary layer top and in the middle and upper troposphere.

In order to further investigate the model microphysical results in both space and time, they were compared with the airborne measurements which were available within the lower cloud formation (I). Airborne observations are the only existing source of direct cloud microphysical
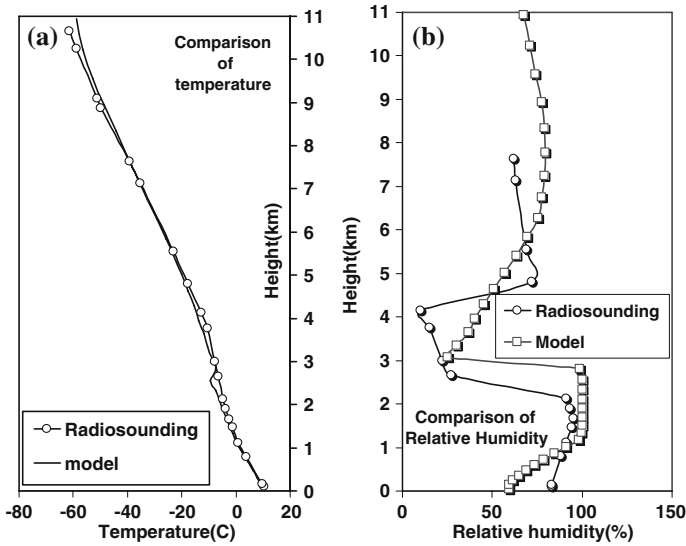
Fig. 14 Vertical profiles of radiosonde measurements over Brest and modeled values over the corresponding to Brest grid point, valid on 12:00 UTC, 10 November 2000 of: (**a**) temperature (°C) and (**b**) relative humidity (%)

measurements, allowing the direct comparison with the results of atmospheric models. The data was collected during constant-altitude flight legs by the "Merlin IV" aircraft of Meteo-France. As reported, the aircraft flights took place in the west-east axis as the cold front was approaching within a layer from 1300 m up to approximately 4300 m. The airport at Brest was either the start or the termination of each flight. The comparison concerned the number concentration and IWC of frozen water substances larger than 25 microns. The measurements were analyzed over 10-s averaging time intervals, over specific grid points within the model inner domain, coinciding with the area covered by the "Merlin IV" flights, while the model data were extracted over the same grid points at model levels close to the altitudes of the flight legs.

For better comparison of the model results to the measurements, the modeled ice particles were grouped into three size bins according to their diameter, corresponding to the size range of the measuring system (Table 1). There is an overlap between the three bins of the GKSS probes, which makes the division of the modeled particles quite complicate. In particular, measurements of the OAP-2D2-C probe were used for ice water species with diameters ranging between 25 and 400 microns, while the measurements of the OAP-2D2-P were used for particle diameter greater than 400 microns.

Scatterplots of model and aircraft IWC and number concentration (N_t) values of medium size particles are displayed in Fig. 15a and b respectively. Even though the modeled values of ice water substances were comparable to those derived from the airborne data (e.g., the simulated IWC reached a value of 0.193 g/m^3 while the measurements were up to 0.19 g/m^3), this comparison showed that the model underestimates both the IWC and the concentration. The underestimation was approximately 17% for IWC with correlation coefficient (R^2) equal to 0.738 (Fig. 15a). For the same time period the simulated concentrations tend to be lower than the observations of about 24% with R^2 equal to 0.9469 (Fig. 15b). The model values were between 0.1 and 249 l^{-1}, while the measured values ranged from 0.9277 up to 330 l^{-1}.
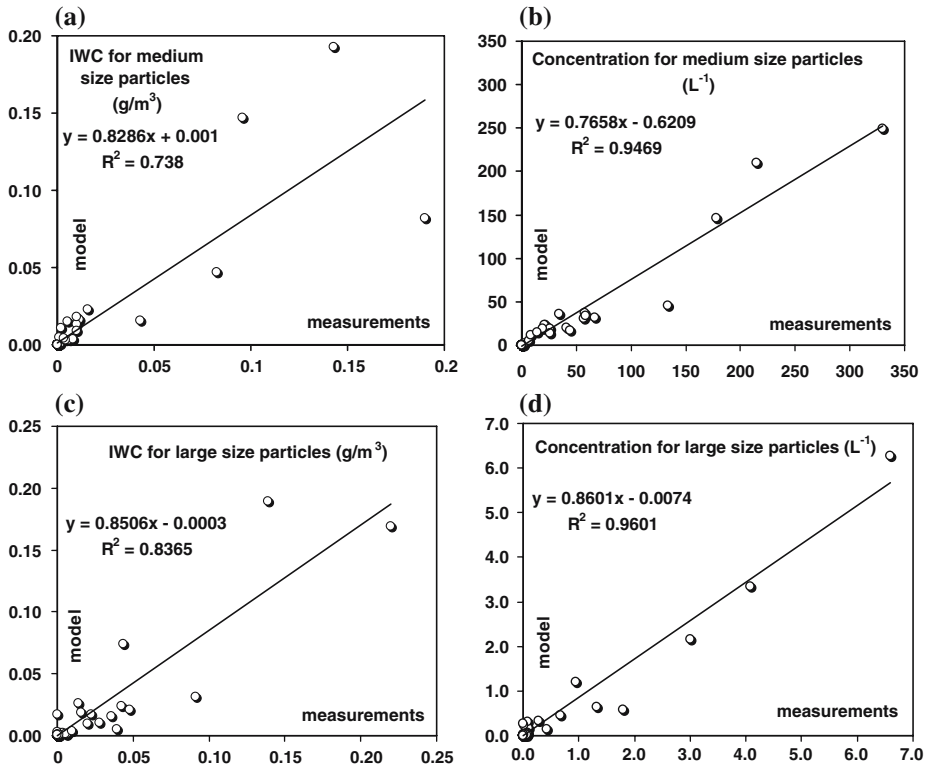
Fig. 15 (**a**) RAMS simulated IWC values versus measured IWC derived from OAP-2D2-C probe, for medium size ice particles (diameters between 25 and 400 microns), (**b**) the same as (**a**), but for number concentration, (**c**) RAMS simulated IWC values versus measured IWC derived from OAP-2D2-P probe, for large size ice particles (diameters greater than 400 microns) and (**d**) the same as (**c**), but for number concentration. The solid curve represents the least square regression line. The least square line equation and the square of the linear correlation coefficient (R^2) are also shown

A similar comparison was also made concerning particles with diameter greater than 400 microns (large size particles/Figs. 15c, d). As it is shown in Fig. 15c, the simulated IWC tends to be lower than the observations of about 15% with R^2 equal to 0.8365. The maximum simulated IWC was 0.189 g/m^3, while the measured one reached a value of 0.22 g/m^3. For the number concentration the underestimation was approximately 14% with correlation coefficient (R^2) equal to 0.9601. The maximum simulated concentration was 6.281^{-1}, while the measured one reached a value of 6.61^{-1}.

In this study, the characteristics of small size particles in the range 2–47 μm diameter were measured by an Forward Scattering Spectral (FSSP-100) probe (see Table 2). The FSSP is designed to measure droplet characteristics although it responds significantly to ice particles. In fact, the response time of the electronics causes several problems, including failure to distinguish between ice particles and liquid droplets. As it is discussed by Gardiner and Hallet [51] false counts due to ice particles could be as high as two or three orders of magnitude greater than the actual ice crystal number concentration, while McFarquhar and Heymsfield [52] note that distributions are of poor quality when large non-spherical ice is present. Recent laboratory investigations strongly suggest that the FSSP counts both small (D < 50 microns) ice particles and cloud drops with equal efficiency (Arnott et al. [53]).

The measurements in this case study showed large occurrence of particles of small diameter, probably due to water layers, as it was indicated by the measured total and liquid water contents (not shown). Specifically, the existence of water is confirmed by measurements of LWC, which reached 1 g/m^3 at 1990 m ASL. The typical values of liquid water contents (LWC) within similar cloud formations range from 0.05 to 0.25 g/m^3 (Cotton and Anthes [45]), though, as they mention, some maxima of over 0.6 g/m^3 have been reported. The model has successfully reproduced these high values of LWC within the lower cloud formation. According to the model results, the LWC of small cloud droplets was, at these heights, between 0.7 and 1.0 g/m^3 after 13:00 UTC (Fig. 10d). On the contrary, the calculated by the model IWC and concentration of small ice particles were extremely low. As it is suggested by Lawson et al. [48], most ice particles grow rapidly to recognizable and non-spherical shapes of larger than 25 μm in less than a minute in mixed-phase clouds. This gives us some confidence that, regardless the fact that there may be some interference on the FSSP measurements by small ice particles, the FSSP instrument may have captured nearly all of the cloud liquid water droplets. Nevertheless, further work is required for extracting solid conclusions on small size water substances.

No comparison between model outputs and data from flights between 3.5 and 4.5 km is presented, due to the model's high underestimation of the cloud microphysical parameters within the bottom boundary of the upper cloud layer. Including these flight levels in the comparison analysis, the correlation between the model data and aircraft observations is poor (not shown). In general, during the afternoon hours, the structure of the vertical layer in the mid troposphere was not accurately described by the model. This should be possibly attributed to the inaccurate representation of the upper part of the cloud deck due to the relatively low model vertical resolution (grid spacing etc.) or to the model's limited capability near the cloud boundaries, which was also observed on the 4 May 1999 cold cloud formation case study of the CARL project (Mavromatidis and Kallos [54]). Another deviation from the observations was that the modeled liquid water was not as significant above 2.5 km, as was suggested by the observed super-cooled water. In this case the model microphysics scheme failed to reproduce the super-cooled water formation below the threshold of −8°C and resulted in the LWC shape shown in Figs. 10c, d.

All the deviations mentioned above may be attributed either to uncertainties of Meyer's formula or to inaccuracies of the measuring system or both. In addition, the influence of the aircraft carrying the probes might have played a role. The quality of airborne probing is strongly affected by the aerodynamic disturbance caused—in the area under consideration—from the aircraft. The trajectories of particles of various shapes and sizes are influenced by the airflow around the aircraft according to their inertia and aerodynamic characteristics. They may cross each other increasing the probability of collision between an ice particle and a supercooled drop so as to initiate the nucleation procedure. To simulate this situation, the airflow around the aircraft was computed using an in house panel method based aerodynamic code and then it was checked numerically that trajectories of particles of various shapes and sizes can effectively cross each other, as it is shown in the next Sect. 4.3.

4.3 Particle trajectories

The particle equation of motion is:

$$m_P \frac{d\vec{V}_P}{dt} = \vec{F}_{AER} + \vec{F}_B + \vec{F}_A + \vec{F}_I + \vec{F}_O + \vec{F}_{OR} + \vec{W}_P \qquad (7)$$

where: m_P = particle mass

V_P = particle velocity at any point of its trajectory

F_{AER} = aerodynamic force

F_B = Basset force (depends on the history of the particles motion)

F_A = Archimedes force

F_I = force due to the inertia of the displaced fluid (by the particle)

F_O = force due to the existence of a transversal velocity gradient regarding to the particle direction of motion

F_{OR} = force due to the attitude of the particle regarding to the local flow direction

W_P = particle weight

A first estimation shows that, all forces are negligible, compared to F_{AER} and W_P (Guffond [55]). F_{AER} is due to the particle inertia, which forces the particle to move slower than the local flow and its module is:

$$F_{AER} = \frac{1}{2}\rho_{AIR}S_P C_D(V_f - V_P)^2 \tag{8}$$

where: ρ_{AIR} = air density at the considered flight level

S_P = particle frontal area

C_D = particle drag coefficient (depends on the particle habit)

V_f = local flow velocity

The particle drag coefficient corresponds to the parasite drag where friction and form drag are included. This coefficient is calculated as a function of the Reynolds number and of the habit of the particle (Clift et al. [56], Beard [57], Auer and Veal [58]). It is also assumed that the particle can respond spontaneously to any local flow direction change, so its frontal surface is always normal to the local flow direction.

According to the above, the particle equation of motion is:

$$m_p \frac{d\vec{V}_p}{dt} = \frac{1}{2}\rho_{AIR}S_P C_D \frac{(\vec{V}_f - \vec{V}_p)}{|\vec{V}_f - \vec{V}_p^|}|\vec{V}_f - \vec{V}_p|^2 + \vec{W}_p \tag{9}$$

which is solved step-by-step using a 4th order Runge–Kutta scheme. The dependence of the Eq. 9 on the local flow velocity V_f requires that the flow characteristics at any point around the probe (so around the aircraft) must be known.

The aerodynamic flow field around the aircraft must be known as a function of the aircraft's geometry, flight speed, attitude (angle of attack), and sideslip angle. It should be noted that in the aircraft's geometry the shape of the probes, as well as their exact location on the aircraft are also included.

Due to the complex geometry involved, only a numerical approach is possible. There are well known numerical approaches where the air is considered either as a viscous or a non-viscous fluid, but in any case the geometry must be described by points combined in order to form elementary surfaces, which approximate the surface of the aircraft. Depending on the approach, the flow field parameters are computed for given flight conditions using Navier–Stokes equations (viscous approach), Euler equations or a Singularities method (non-viscous approach).

In the case of Navier–Stokes and Euler equations a grid must be generated on and around the aircraft at each node of which the flow parameters are computed. This approach demands high memory capacity, it is time consuming and it is not always converging. On the other hand, there is no need for grid around the aircraft in the case of Singularities method (see for instance Katz and Plotkin [59]). This approach is not very demanding in memory capacity and is generally fast converging. For this reason it was adopted in our case. The aircraft was flown at cruising speed so at low angle of attack, so its boundary layer thickness is negligible

Table 7 Starting points of trajectories of various cloud particles converging at the same point (head of the probe)

Type	Water drops	Water drops	Hexagon. columns	Hexagon. columns	Cylin. columns	Cylin. columns	Disks
D (μm)	100	200	100	200	100	200	400
Xinit (m)	0.0	0.0	0.0	0.0	0.0	0.0	0.0
Yinit (m)	−5.1583	−5.1859	−5.1757	−5.1757	−5.1708	−5.1708	−5.1355
Zinit (m)	−1.0840	−1.0829	−1.0841	−1.0842	−1.0845	−1.0845	−1.0880

compared to its dimensions and no flow separation occurs. This allows for the use of a vortex panel code for the calculation of the flow field around the aircraft.

Several runs were made in order to prove that trajectories of ice particles and water drops of various sizes starting from different points will cross each other at a given point (in our case this point is located in front of the probe). In Table 7 the starting points of trajectories of water drops and ice crystals of various shapes and of 100 μm, 200 μm and 400 μm of diameter converging at a point in front of the probe are shown. Those diameters were chosen because particles of those sizes were found during the measurements and to fulfil the requirements found experimentally and theoretically (Pitter and Pruppacher [60], Schlamp et al. [61]). The fact, that these trajectories can cross each other, means that the corresponding cloud particles may collide leading to ice crystals rimming and to an increase of the IWC in the real cloud. This fact could partially explain the underestimation of IWC by the RAMS model, but further investigation is needed in order to validate this explanation.

5 Summary and conclusions

On 10 November 2000, a low pressure system over North Atlantic advected maritime type of air masses towards the western coast of France. In the area of Brest, low cloud formation associated with rain was modeled as part of the warm front. The GKSS polarimetric radar detected for the time period from 06:00 to 15:00 UTC two well-defined cloud bands. The lower one reached altitudes up to 2 or 3 km and the second one extended between 3.5 and 10 km. In this paper an attempt was made to describe various microphysical cloud properties with the aid of the atmospheric model RAMS and through conventional atmospheric observations. The RAMS modeling system was used in hindcasting mode, while an independent data set based on the GKSS radar observations and on aircraft measurements ("Merlin IV") was used for model validation.

The model simulations showed that the lower cloud formation (top at 2.5 km) was characterized by high number concentration of pristine ice and snow and lower concentration of aggregates, graupel and hail. Hydrometeors in liquid phase prevailed in the layer extending from the ground up to about 2.5 km with high number concentration and water content (LWC) at the top of this layer. The altitude of the freezing level (observed and calculated) suggests that the liquid water resulted not only by the warm cloud formation mechanisms, but also by the melting of ice hydrometeors, as was clearly shown by the radar data.

The calculated temperature and humidity fields compare well to the radiosonde measurements performed at the airport of Brest. The comparison with the available observational data (radar reflectivity) showed that the model described fairly well the vertical structure of

the cloud formation. The temporal variability of the cloud parameters was also successfully simulated. However, the model did not accurately reproduce the mid-tropospheric cloud formation during the afternoon hours since the model predicted insignificant quantities of liquid and ice between 3.5 and 4.5 km, where a super-cooled water layer was observed.

The comparison between model values and aircraft data for the small-size particles is considered as meaningless. This is because of the uncertainties in the measurements related to the FSSP measuring system and the model's disability to reproduce amounts of small ice particles comparable to the measurements. On the contrary, the model reproduced large amounts of small particles in liquid phase. As for the medium and large size particles, the simulated IWC and number concentration values were found to compare fairly well to those derived by the measurements, despite the fact that the model underestimates both of these parameters. For the medium-size particles, the model values of IWC were approximately 17% lower than those of the measurements, while the corresponding percentage for N_t was approximately 24%. For the large-size particles, the model underestimated both the IWC and the number concentration by approximately 15% in comparison to the aircraft data. These deviations may be attributed either to the model parameterization or to inaccuracies in the measuring system. The disturbance created by the presence of the aircraft during the airborne probing within the mixed phase cloud may have also played an additional role for this discrepancy.

In general, the model performance is considered to be satisfactory to a certain degree. However, the deviations of the modeled quantities from the measured ones clearly indicate that the model parameterization of cloud processes requires further investigation and development in order to accurately describe the entire factors and mechanisms controlling the cloud formation and evolution especially for the small size particles.

References

1. Kain JS, Fritsch JM (1990) A one-dimensional entraining/ detraining plume model and its application in convective parameterization. J Atmos Sci 47(23):2784–2802
2. Tremback CJ (1990) Numerical simulation of a mesoscale convective complex: model development and numerical results. Ph.D. dissertation, Atmos Sci Paper No. 465, Colorado State University, Dept of Atmos Science, Fort Collins, Co 8523.
3. Pielke RA, Cotton WR, Walko RL, Tremback CJ, Lyons LD, Grasso WA, Nicholls ME, Moran MD, Wesley DA, Lee TJ, Copeland JH (1992) A comprehensive meteorological modeling system - RAMS. Meteorol Atmos Phys 49:69–91
4. Wang C, Chang JS (1993) A three-dimensional numerical model of cloud dynamics, microphysics and chemistry. 1: Concepts and formulation. J Geophys Research 98(D8):14827–14844
5. Heckman ST, Cotton WR (1993) Mesoscale numerical simulation of cirrus clouds–FIRE case study and sensitivity analysis. Mon Wea Rev 121:2264–2284
6. Chen J-P (1994) Notes and Correspondence: Prediction of saturation ratio for cloud microphysical models. J Atmos Sci 51(10):1332–1338

7. Stevens B, Cotton WR, Feingold G (1998) A critique of one- and two-dimensional models of boundary layer clouds with a binned representation of drop microphysics. J Atmos Res 47–48:529–533
8. Bernardet LR, Cotton WR (1998) Multi–scale evolution of a derecho–producing MCS. Mon Wea Rev 126:2991–3015
9. Harrington JY, Reisin T, Cotton WR, Kreidenweis SM (1999) Cloud resolving simulations of Arctic stratus. Part II: Transition – season clouds. Atmos Res 51:45–75
10. Wu T, Cotton WR, Cheng WYY (2000) Radiative effects on the diffusional growth of ice particles in cirrus clouds. J Atmos Sci 57:2892–2904
11. Jiang H, Cotton WR (2000) Large–eddy simulation of shallow cumulus convection during BOMEX: sensitivity to microphysics and radiation. J Atmos Sci 57:582–594
12. Jiang H, Cotton WR, Pinto JO, Curry JA, Weissbluth MJ (2000) Cloud resolving simulations of mixed-phase Arctic stratus observed during BASE: Sensitivity to concentration of ice crystals and large – scale heat and moisture advection. J Atmos Sci 57:2105–2117
13. Mace GG, Starr DO'C, Ackerman TP, Minnis P (1995) Examination of coupling between an upper – tropospheric cloud system and synoptic – scale dynamics diagnosed from wind profiler and radiosonde data. J Atmos Sci 5:4094–4127
14. Brown PRA, Swann HA (1997) Evaluation of key microphysical parameters in three–dimensional cloud–model simulations using aircraft and multiparameter radar data. Quart J Roy Meteor Soc 123:2245–2275
15. Guan H, Cober SG, Isaac GA (2001) Verification of supercooled water forecasts with in situ aircraft measurements. Wea Forecasting 16:145–155
16. Guan H, Cober SG, Isaac GA, Tremblay A, Methot A (2002) Comparison of three cloud forecast schemes with in situ aircraft measurements. Wea Forecasting 17:1226–1235
17. Nasiri SL, Baum BA, Heymsfield AJ, Yang P, Poellot MR, Kratz DP, Hu Y (2002) The development of midlatitude cirrus models for MODIS using FIRE-I, FIRE-II, and ARM in-situ data. J Appl Meteor 41:197–217
18. Lekas ITh, Mavromatidis E, Kallos G (2006) Some considerations on the airborne cloud microphysical probing. Meteorol Atmos Phys 92:217–230, published online: December 22, 2005
19. Snook JS, Stamus PA, Edwards J, Christidis Z, McGinley JA (1998) Local–domain analysis and forecast model support for the 1996 centennial Olympic Games. Wea Forecasting 13:138–150
20. Powell MD, Rinard SK (1998) Marine forecasting at the 1996 centennial Olympic Games. Wea Forecasting 13:764–782
21. McQueen JT, Valigura RA, Stunder BJB (1997) Evaluation of the RAMS model for estimating turbulent fluxes over the Chesapeake Bay. Atmos Environ 31:3803–3819
22. Case LJ, Manobianco J, Dianic AV, Wheeler MM, Harms DE, Parks CR (2002) Verification over East – Central Florida during the 1999 and 2000 Summer Months. Wea Forecasting 17:1133–1151
23. Warren GS, Hahn CJ, London J (1985) Simultaneous occurrence of different cloud types. J Climate Appl Meteor 24:658–667
24. Tian L, Curry JA (1989) Cloud overlap statistics. J Geophys Res 94:9925–9935
25. Pelon J, Testud J, Noel V, Tinel C, Guyot A, Caillaud K, Protat A, Chepfer H, Trouillet V, Baudin F, Flamant H, Quante M, Nagel D, Lemke H, Danne O, Albers F, Raschke E, Kallos G, Mavromatidis E (2001) Investigation of cloud by ground-based and airborne radar and lidar (CARL). Final Report for the European Commission, DGXII, Contract PL-970567
26. Cotton WR, Pielke RA Sr, Walko RL, Liston GE, Tremback CJ, Jiang H, McAnelly RL, Harrington JY, Nicholls ME, Carrio GG, McFadden JP (2002) RAMS 2001: current status and future directions. Meteor Atmos Phys 82:5–29
27. Smagorinsky J (1963) General circulation experiments with the primitive equations. Part I, The basic experiment. Mon Wea Rev 91:99–164
28. Hill GE (1974) Factors controlling the size and spacing of cumulus clouds as revealed by numerical experiments. J Atmos Sci 31:646
29. Lilly DK (1962) On the numerical simulation of buoyant convection. Tellus, XIV 2:148–172
30. Walko RL, Cotton WR, Meyers MP, Harrington JY (1995) New RAMS cloud microphysics parameterization. Part I: the single moment scheme. Atmos Res 38:29–62
31. Harrington JY, Meyers MP, Walko RL, Cotton WR (1995) Parameterization of ice crystal conversion processes due to vapor deposition for mesoscale model using double-moment basis functions. Part I: Basic formulation and parcel model results. J Atmos Sci 52:4344–4366
32. Meyers MP, Walko RL, Harrington JY, Cotton WR (1997) New RAMS cloud microphysics parameterization. Part II: The two-moment scheme. Atmos Res 45:3–39
33. Flatau PJ, Tripoli GJ, Verlinde J, Cotton WR (1989) The CSU-RAMS cloud microphysical module: general theory and code documentation. Colorado State Univ., Dep Atmos Sci, Fort Collins, Colorado 80523, Atmos Sci Pap, 451, 88 pp

34. Verlinde J, Flatau PJ, Cotton WR (1990) Analytical solutions to the collection growth equation: Comparison with approximate methods and application to cloud microphysics parameterization schemes. J Atmos Sci 47:2871–2880
35. Meyers MP, DeMott PJ, Cotton WR (1992) New primary ice-nucleation parameterization in an explicit cloud model. J Appl Meteor 33:617–626
36. DeMott PJ, Meyers MP, Cotton WR (1994) Parameterization and impact of ice initiation processes relevant to numerical model simulations of cirrus clouds. J Atmos Sci 51:77–90
37. Mossop SC (1978) The influence of drop size distribution on the production of secondary ice particles during graupel growth. Q J Roy Meteor Soc 104:323–330
38. Klemp JB, Wilhelmson RB (1978) The simulation of three-dimensional convective storm dynamics. J Atmos Sci 35:1070–1096
39. Kain JS, Fritsch JM (1993) Convective parameterization for mesoscale models: The Kain–Fritsch scheme. The representation of cumulus convection in numerical models of the atmosphere. Meteor Monogr No 46, Amer Meteor Soc 165–170
40. Chen C, Cotton WR (1987) The physics of the marine stratocumulus-capped mixed layer. J Atmos Sci 44:2951–2977
41. Walko RL, Band LE, Baron J, Kittel TGF, Lammers R, Lee TJ, Ojima D, Pielke RA Sr, Taylor C, Tague C, Tremback CJ, Vidale PL (2000) Coupled atmosphere-biophysics-hydrology models for environmental modelling. J Appl Meteor 39:931–944
42. Krichak SO, Levin Z (2000) On the cloud microphysical processes during the November 2, 1994 hazardous storm in the southeastern Mediterranean as simulated with a mesoscale model. Atmos Res 53:63–89
43. Houze AR Jr (1993) Cloud dynamics. Academic Press, Inc., International Geophysical Series, vol 53, ISBN: 0-12-356881-1
44. Hobbs PV, Rangno AL, Uttal T, Shupe M (2001) Airborne studies of cloud structures over the Arctic Ocean and comparisons with retrievals from ship-based remote sensing measurements. J Geophys Res 106:15029–15044
45. Cotton WR, Anthes RA (1989) Storm and cloud dynamics. Academic Press, Inc. ISBN: 0-12-192530-7
46. Pruppacher RH, Klett JD (1997) Microphysics of clouds and precipitation (Second revised and enlarged edition), vol 18 Kluwer Academic Publishers, Atmospheric and Oceanographic Sciences Library, ISBN: 0-7923-4211-9
47. Fleishauer RP, Larson VE, Vonder Haar TH (2002) Observed microphysical structure of midlevel, mixed-phase clouds. J Atmos Sci 59:1779–1804
48. Lawson RP, Baker BA, Schmitt CG, Jensen TL (2001) An overview of microphysical properties of Arctic clouds observed in may and July during FIRE. J Geophys Res 106:14989–15014
49. Albrecht BA, Randall DA, Nicholls S (1988) Observations of marine stratocumulus clouds during FIRE. Bull Amer Meteor Soc 69:618–626
50. Bretherton CS, Pincus R (1993) Cloudiness and marine boundary layer dynamics in the ASTEX Langragian experiment. Part I: Synoptic setting and vertical structure. J Atmos Sci 52:2707–2723
51. Gardiner BA, Hallett J (1985) Degradation of in-cloud forward scattering spectrometer probe measurements in the presence of ice particles. J Atmos Ocean Technol 2:171–180
52. McFarquhar GM, Heymsfield AJ (1996) Microphysical characteristics of three anvils sampled during the Central Equatorial Pacific Experiment (CEPEX). J Atmos Sci 53:2401–2423
53. Arnott WP, Mitchell D, Schmitt C, Kingsmill D, Ivanova D (2000) Analysis of the FSSP performance for measurement of small crystal spectra in cirrus. In: Proceedings 13th international conference on clouds and precipitation, Reno, NV, ICCP, pp 191–193
54. Mavromatidis E, Kallos G (2003) An investigation of cold cloud formation with a three dimensional model with explicit microphysics. J Geophys Res 108(D14):4420–4450
55. Guffond D (1981) Ice accretion on a protected surface during a flight in icing conditions. (In French). ONERA, RT, no 3/5146 SY
56. Clift R, Grace JR, Weber ME (1978) Bubbles, drops and particles. Academic press
57. Beard KV (1976) Terminal velocity and shape of cloud precipitation drops aloft. J Atmos Sci 33:851–864
58. Auer AH Jr, Veal DL (1970) The dimension of ice crystals in natural clouds. J Atmos Sci 27:919–926
59. Katz J, Plotkin A (1991) Low speed aerodynamics. Mc Graw-Hill Publishers
60. Pitter RT, Pruppacher HR (1974) A numerical investigation of collision efficiencies of simple ice plates colliding with supercooled water drops. J Atmos Sci 31:551–559
61. Schlamp R, Pruppacher HR, Hamielec AC (1975) A numerical investigation of the efficiency with which simple columnar ice crystals collide with supercooled water drops. J Atmos Sci 32:2330–2337